A Novel Multi-electrode Sensing Strategy for Electrical Capacitance Tomography with Ultra-low Dynamic Range

A Novel Multi-electrode Sensing Strategy for Electrical Capacitance Tomography with Ultra-low Dynamic Range

Yunjie Yang[a*], Lihui Peng[b] and Jiabin Jia[a]

a Agile Tomography Group, School of Engineering, The Univeristy of Edinburgh, Edinburgh, EH9 3JL, UK
b Department of Automation, Tsinghua University, Beijing, 100084, China
** Email: y.yang@ed.ac.uk*

Abstract

Common sensing strategy of Electrical Capacitance Tomography (ECT) is to measure the capacitances across all independent combinations of individual electrodes. The capacitance values from conventional sensing strategies usually have large dynamic ranges and severe nonlinear effect in reconstructed images when using linearized ECT model, thus making it difficult to obtain satisfactory images. In this paper, a novel multi-electrode sensing strategy for ECT with ultra-low dynamic range is reported to offer improved solutions regarding these problems. The proposed sensing strategy takes advantage of the flexibility of combining electrode method, while a new opposite multi-electrode simultaneous asymmetric excitation and measurement protocol is further developed. A 24-electrode ECT sensor is selected as the basic sensor, and a pair of asymmetrically opposite electrodes are excited in a simultaneous manner. The proposed sensing strategy can significantly decrease the dynamic range of measurements compared with our former reported work. Moreover, nonlinear effect is weaker compared with that of conventional sensing strategy when performing linearized-model-based image reconstruction. To validate the proposed sensing strategy, modelling of 3D ECT sensors and numerical analysis are carried out. The proposed strategy is characterized from the aspects of capacitance measurement, compression ratio, dynamic range, sensitivity map, and quality of reconstructions. Additionally, preliminary experimental validation is also conducted. Both simulation and experiment results indicate significantly improved sensing characteristics and quality of reconstructed images. The novel sensing strategy will lead to a lower burden for capacitance measurement circuit and better quality of tomographic image.

Keywords: Electrical Capacitance Tomography; multi-electrode sensing; simutaneous asymetric excitation; image reconstruction

1. Introduction

Electrical Capacitance Tomography (ECT) is one of the industrial process tomography modalities. Its working principle is to measure capacitances between sensor electrode pairs and estimate the permittivity distribution inside pipelines or vessels via a visualized manner [1]. Attributing to its advantages of non-invasiveness, non-radiation, high temporal resolution, economy and usability, ECT has been widely studied and applied to reveal process characteristics. Numerous successful cases have been reported, including fluidized bed monitoring [2], gas/oil/water multi-phase flow measurement [3], flow velocity measurement [4], and flame imaging [5], etc. In spite of its superiority and potential, problems emerging from capacitance measurement and data acquisition system development, capacitive sensor design and optimization, and image reconstruction algorithm study still remain to be solved in order to make ECT a better tomographic technique. In the past decades, progress has been continuously made regarding these issues, such as high-speed digital ECT systems development [6-7], rotating electrode sensing strategy study [7-8], and novel image reconstruction algorithms investigation [9-12]. While the image reconstruction algorithms and ECT system development are continuing to mature, the alterative sensing strategy with better performance has not been sufficiently studied yet.

The work in this paper aims at improving current ECT sensing strategies. Common ECT sensing strategy is to sense the capacitances formed by all independent sensor electrode pairs [9]. In most publications, the 8-electrode, 12-electrode or 16-electrode ECT sensor is applied. A recently published work suggests that the 12-electrode sensor demonstrates the best performance among conventional ECT sensing strategies, and simply increasing the number of electrodes in an ECT sensor results in limited improvement [13]. However, conventional ECT sensor structure has problems such as large dynamic range of capacitance measurements. It incurs great challenge for capacitance

measurement circuit. Moreover, in linearized-ECT-model-based image reconstruction, distortion or artifact caused by nonlinear effect is evident for many permittivity patterns if capacitance data from all electrode pairs are used [11]. The existing problems make it difficult to produce stable and high quality tomographic images.

In former reported work [7], the authors have symmetrically investigated an alternative sensing solution using a combining electrode strategy and the development of an ECT system supporting the combining strategy. The feasibility of combining electrode sensing was verified in both theoretical and practical aspects, and several potential combining electrode strategies were proposed and validated. Although the dynamic range of measurements are reduced from around 504 to around 63, it is still large compared with that of conventional 8-electrode sensing strategy, which is around 43.

Work in this paper aims at further reducing the dynamic range while preserving other advantages of combining electrode method. A Multi-electrode Asymmetric Sensing Strategy (MASS) for ECT with ultra-low dynamic range is proposed. The proposed sensing strategy takes advantage of the hardware flexibility of combining electrode method to reform conventional sensitivity distributions, while a novel simultaneous opposite multi-electrode asymmetric excitation and adjacent measurement protocol is further developed. In the proposed sensing protocol, a 24-electrode ECT sensor is selected as the basic sensor. Different from reported sensing strategies, a pair of asymmetrically opposite electrodes are excited in a simultaneous manner and the measurement is taken from two combining electrodes at the same time. The MASS is able to significantly reduce the dynamic range of capacitance measurements and meanwhile preserve enough information for image reconstruction. To characterize MASS, the aspects of capacitance measurement, compression ratio, dynamic range, sensitivity map, and quality of reconstructions are investigated. Both simulation and experiment are carried out to verify the feasibility and image quality of MASS, and promising results have been obtained.

The paper is organized as follows. In Section 2, the principle of ECT, multi-electrode sensing as well as the MASS are presented and then the characteristics of MASS are investigated based on 3D simulation. In Section 3, image reconstruction of four simulated permittivity phantoms and three real phantoms are conducted based on the given one-step and iterative algorithms. Image quality analysis and comparison with 12-electrode and 24-electrode methods are also performed in this section. Finally, conclusions and future work are summarized, and several remarks regarding multi-electrode sensing are given in Section 4.

2. Multi-electrode Asymmetric Sensing Strategy

2.1. Principle of ECT and multi-electrode sensing

Fig.1 shows the schematic illustration of a conventional 12-electrode ECT sensor.

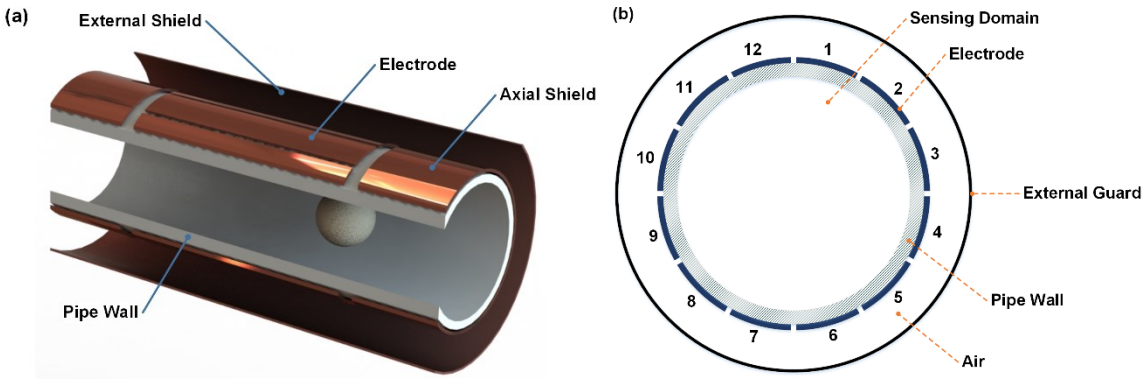

Fig. 1. Schematic illustration of conventional 12-electrode ECT sensor. (a) 3D view; (b) 2D cross section.

ECT measures capacitances between all electrode pairs and then the data together with a pre-calculated sensitivity map (also referred to as the Jacobian matrix) are employed to estimate the 3D or cross-section permittivity change within the region of interest. A linearized model describing the relationship between capacitance vector and permittivity change vector is expressed as [9]:

$$\vec{\lambda} = \bar{S}\vec{g} \tag{1}$$

where $\vec{\lambda}$ is the normalized capacitance vector; $\bar{S}$ is the normalized sensitivity matrix; $\vec{g}$ is the normalized permittivity change vector with respect to the two-end calibrations [9]. As a typical inverse problem, the target of ECT reconstruction is to estimate $\vec{g}$ based on $\vec{\lambda}$ and $\bar{S}$. Commonly used ECT image reconstruction algorithms have been summarized in a review paper [9].

In a typical ECT sensing strategy, a single-electrode excitation and single-electrode measurement method is successively adopted to obtain all the capacitance data among all the electrodes. However, there are problems in this method. For instance, high hardware requirement because of large dynamic range of measurement, varying linearization error between different capacitance groups [11], and slow imaging speed, etc. In order to figure out these problems, a series of preliminary trial regarding combining electrode strategy were carried out and reported by the authors [7]. While in these work, only single combining electrode is utilized as excitation which has limited effect on reducing the dynamic range. In this work, a novel ECT sensing strategy, MASS, is came up with to address this problem. In MASS, a pair of asymmetric combined electrodes are excited simultaneously. Fig. 2 shows the schematic illustration of the MASS. A pair of opposite combined electrodes A1 and A2 are excited simultaneously, and each combined electrode is formed by several single electrodes. Meanwhile, a combined electrode B formed by two single electrodes acts as the measurement.

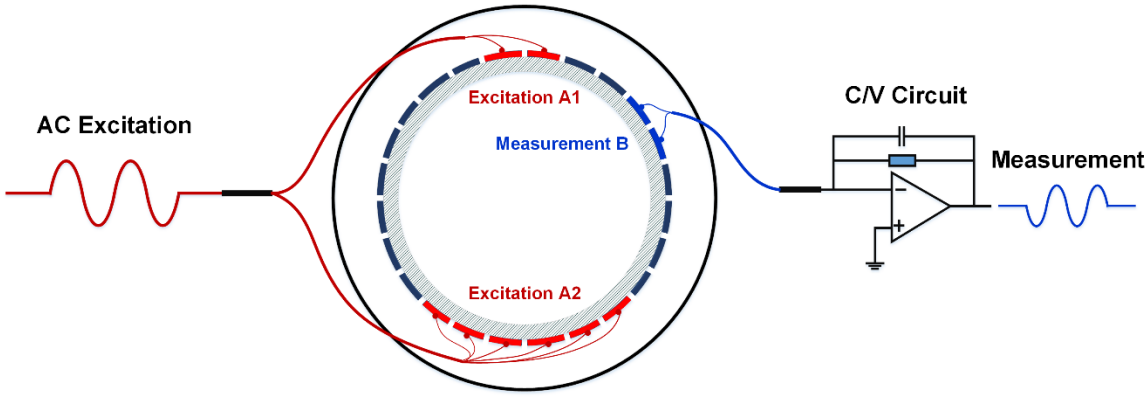

Fig. 2. Schematic illustration of the MASS.

According to the authors' work in [7], the capacitance formed by the excited combined electrode [A1, A2] and combined measurement electrode B equals to the linear superposition of all the capacitances formed by each individual electrode of [A1, A2] and B. A matrix is utilized to denote the linear superposition of combining electrode capacitance from individual electrode capacitance. Furthermore, considering the capacitance data of general multi-electrode sensing strategy for one frame image reconstruction, it can be expressed as:

$$\overline{C}_{m[l\times 1]} = \begin{bmatrix} 1 & 1 & \cdots & \\ 0 & 0 & \cdots & \\ \vdots & \vdots & \ddots & \vdots \ \vdots \\ 1 & 0 & \cdots & \\ 0 & 1 & \cdots & \end{bmatrix}_{[l\times n]} \overline{C}_{s[n\times 1]} = \bar{L}_{[l\times n]}\overline{C}_{s[n\times 1]} \tag{2}$$

where $\overline{C}_m$ is a completed frame of capacitance data obtained from a multi-electrode sensing strategy, which data length is l; $\overline{C}_s$ is a completed frame of capacitance data obtained from conventional sensing strategy using the same sensor, which data length is n, and for an ECT sensor with N electrodes, $n = C_N^2$; $\bar{L}$ is the linear superposition matrix calculated based on the multi-electrode sensing strategy, which means each capacitance measurement in $\overline{C}_m$ is the linear superposition of certain capacitance measurements in $\overline{C}_s$. Here, the subscript expression in bracket indicates the dimension of corresponding vector / matrix. Normally, $l \le n$, but when $\bar{L}$ is the unit matrix, multi-electrode sensing strategy degenerates to conventional sensing strategy.

Consequently, the linearized model for multi-electrode sensing and its normalized form can be expressed as Eq. (3) and Eq. (4) respectively.

$$\begin{aligned}\overrightarrow{C}_{m[obj]} - \overrightarrow{C}_{m[low]} &= \overrightarrow{L}\left(\overrightarrow{C}_{s[obj]} - \overrightarrow{C}_{s[low]}\right) \\ &= \overrightarrow{L}\left(\overrightarrow{J}\overrightarrow{\varepsilon}_{s[obj]} - \overrightarrow{J}\overrightarrow{\varepsilon}_{s[low]}\right) \\ &= \overrightarrow{L}\overrightarrow{J}\left(\overrightarrow{\varepsilon}_{s[obj]} - \overrightarrow{\varepsilon}_{s[low]}\right) \\ &= \overrightarrow{J}_m\left(\overrightarrow{\varepsilon}_{s[obj]} - \overrightarrow{\varepsilon}_{s[low]}\right)\end{aligned} \tag{3}$$

$$\overrightarrow{\lambda}_m = \overrightarrow{S}_m\overrightarrow{g} \tag{4}$$

where $\overrightarrow{C}_{m[obj]}$ and $\overrightarrow{C}_{m[low]}$ are the capacitance data from a multi-electrode sensing strategy when the vessel is filled with high permittivity medium $\overrightarrow{\varepsilon}_{s[obj]}$ and low permittivity medium $\overrightarrow{\varepsilon}_{s[low]}$, respectively; $\overrightarrow{C}_{s[obj]}$ and $\overrightarrow{C}_{s[low]}$ are capacitance data from conventional sensing strategy under the same conditions, respectively; $\overrightarrow{J}$ is the sensitivity matrix of conventional sensing strategy without normalization; $\overrightarrow{J}_m = \overrightarrow{L}\overrightarrow{J}$ is the sensitivity matrix of the multi-electrode sensing strategy without normalization; $\overrightarrow{\lambda}_m$ and $\overrightarrow{S}_m$ are the normalized capacitance data and sensitivity matrix of the multi-electrode sensing strategy, respectively; $\overrightarrow{g}$ is the normalized permittivity change vector. The detailed theoretical derivation from Eq. (2) to Eq. (4) can be referred to [7]. Apparently, Eq. (4) has the same form with Eq. (1) and the same image reconstruction algorithms can be applied.

2.2. Multi-electrode asymmetric excitation sensing strategy

Based on the multi-electrode sensing principle demonstrated from Eq. (2) to Eq. (4), the Multi-electrode Asymmetric Excitation Sensing Strategy (MASS) is proposed. The MASS is implemented based on a 24-electrode ECT sensor. The detailed sensing protocols of MASS are illustrated in Fig. 3.

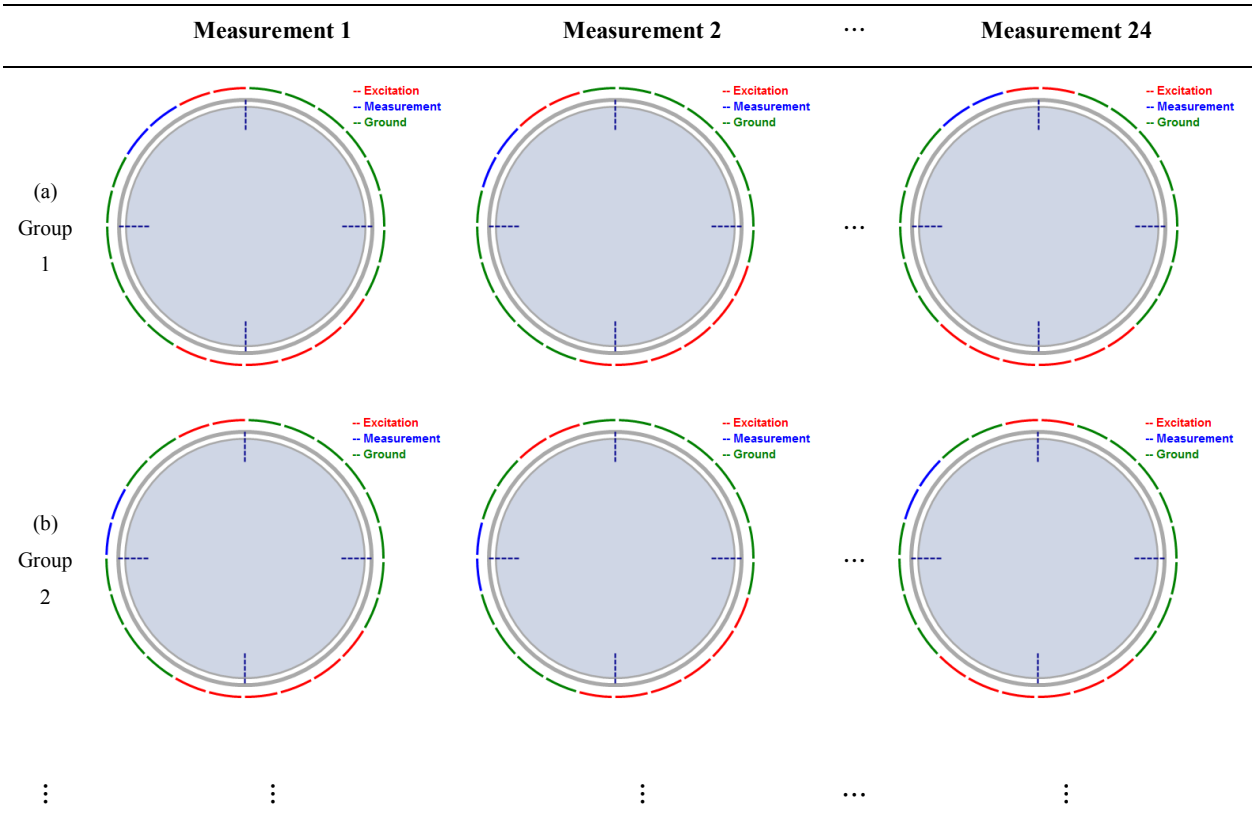

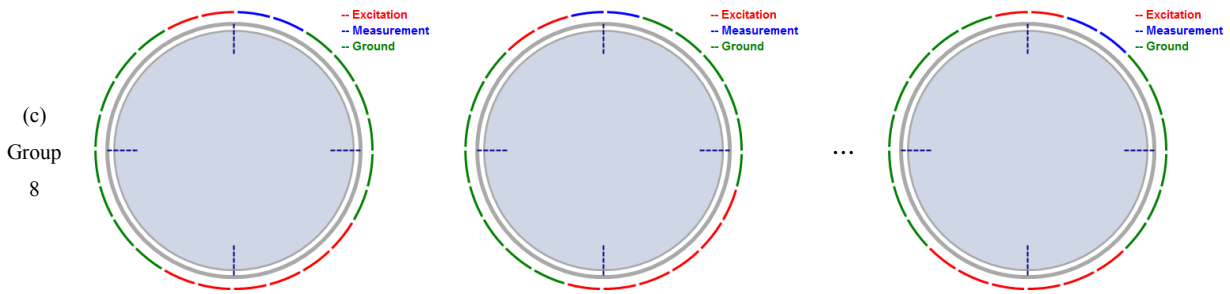

Fig. 3. Sensing protocol of MASS. (a) the first group (w.r.t. left to right figures): start position, counter-clockwise rotation by one electrode, counter-clockwise rotation by 24 electrodes; (b) the second group (w.r.t. left to right figures): start position, counter-clockwise rotation by one electrode, counter-clockwise rotation by 24 electrodes; (c) the eighth group (w.r.t. left to right figures): start position, counter-clockwise rotation by one electrode, counter-clockwise rotation by 24 electrodes.

In MASS, two opposite asymmetric combining electrodes are excited simultaneously, one with two electrodes and the other with six electrodes. The measurement electrodes are consisted of two electrodes. The opposite excitation reduces the capacitance distance (the definition can be referred to [11]), and as a result, the dynamic range of capacitance values is significantly reduced. The asymmetric configuration increases the difference of sensitivity value at different pixel locations of a single measurement compared with the conventional symmetric configuration. The sensing procedure of MASS is as following: the whole excitation and measurement procedure is composed of eight groups, and the first, second and last group are shown in Fig. 3(a), (b), and (c), respectively; each group starts at the position depicted on the left side image and then rotates one electrode anti-clockwise until it rotates 24 times, which is depicted on the right side image. All measurements will be taken to obtain a complete frame capacitance data for image reconstruction. Therefore, the total capacitance measurement number of the proposed strategy is 24×8=192, while the total number of capacitance measurement in a typical 24-electrode sensor is $C_{24}^{2} = 276$.

2.3. Modelling and characterization

The MASS is modelled and characterized in this section by simulation. A 3D ECT sensor with 24 electrodes is modelled to implement MASS, which is illustrated in Fig. 4(a). In addition, for performance comparison with conventional ECT sensor, a 3D 12-electrode ECT sensor is also modelled and characterized, which is shown in Fig. 4(b). The 12-electrode ECT sensor model has the same pipeline dimension and material setup with the 24-electrode sensor. Note that the notation of sensor structure is only shown in Fig. 4(a), while Fig. 4(b) has similar structure but varies in electrode dimension. The dimension and material parameters used in the following sensors and subsequent phantom simulation analysis are demonstrated in Table 1.

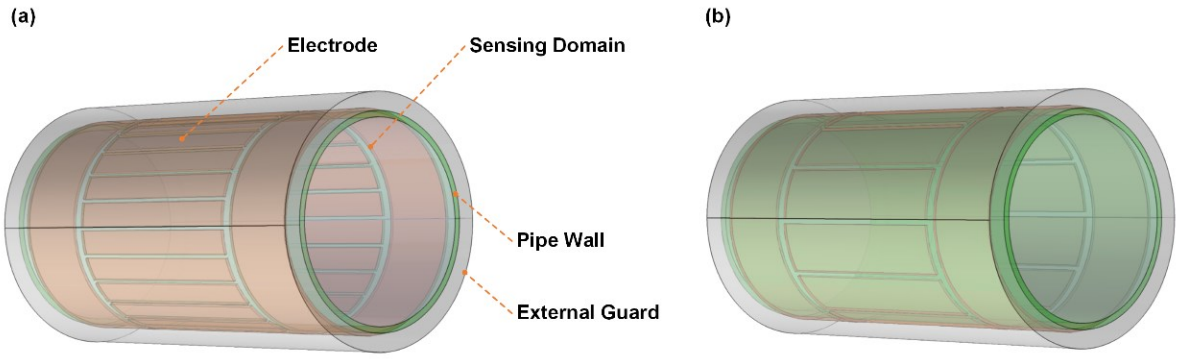

Fig. 4. 3D modelling of ECT sensors. (a) 24-electrode sensor; (b) 12-electrode sensor.

Table 1. Key parameters of the modelled sensors in Fig. 4.

Dimension	**Perimeter**	**Electrode Width**	**Electrode Length**	**Electrode Interval**
	248.06 mm	(a) 9.3 mm (b) 18.6 mm	70 mm	(a) 1.03 mm (b) 2.06 mm
	Pipe Outer Diameter	**Thickness of Pipe Wall**	**Pipe Inner Diameter**	**Guard Width**
	79 mm	2 mm	75 mm	25 mm

Material	**Pipe**	**Electrode & Guard**	**Low Dielectric Medium**	**High Dielectric Medium**
	PVC (ε=2.6)	Copper	Air (ε=1.0)	Sand (ε=3.0)

In order to validate the multi-electrode sensing principle and linearized model for the MASS, distribution of electrical potential of MASS is primarily analyzed. The analysis is carried out on a 2D cut plane in the middle of the electrodes, as shown in Fig. 5.

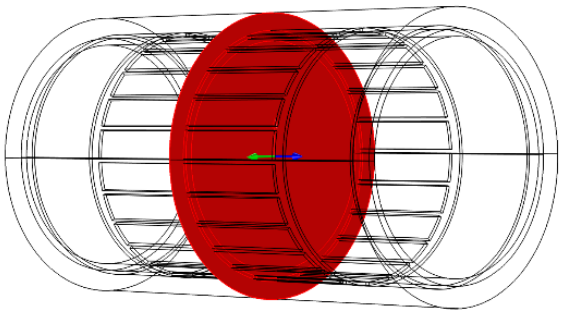

Fig. 5. The position of analyzed 2D cut plane relative to the modelled 24-electrode sensor.

Fig. 6(b) shows the electrical potential distribution when a single electrode in Fig. 6(a) is excited. Fig. 7(b) illustrates the electrical potential distribution when one measurement of the MASS is applied as shown in Fig. 7(a). By applying simultaneous opposite excitation, it is confirmed that the electrical field near the pipe center is greatly enhanced. The electrical potential distribution along a 1D cutline as shown in Fig. 8(a) is further analyzed under the excitation configuration in Fig. 7(a) to validate the linear superposition. Fig. 8(b) shows the comparison of real electrical potential value along the 1D cut line and the calculated electrical potential value based on linear superposition rule. The calculated value is the summary of eight electrical potential values when eight single electrodes in Fig. 7(a) are excited individually. It is shown that the calculated value coincides well with the real electrical potential value, which further validates the underlying multi-electrode sensing principle that supports the derivation of Eq. (4).

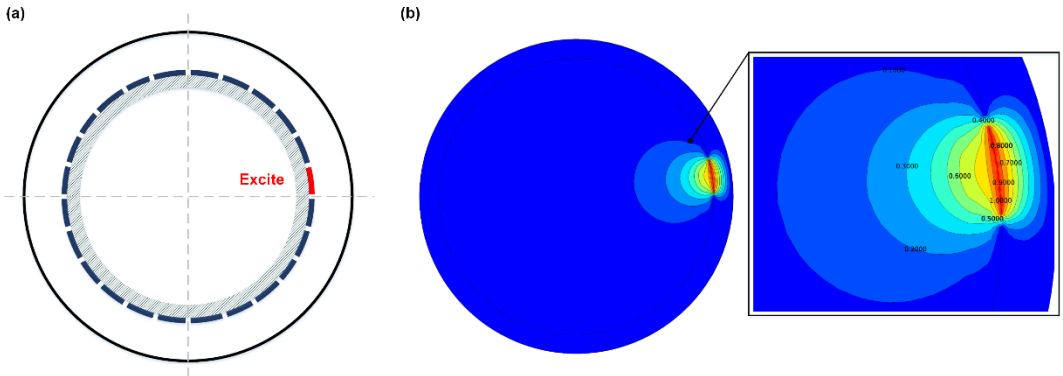

Fig. 6. Electrical potential distribution from single electrode excitation. (a) Position of the excited electrode; (b) Resulting electrical potential.

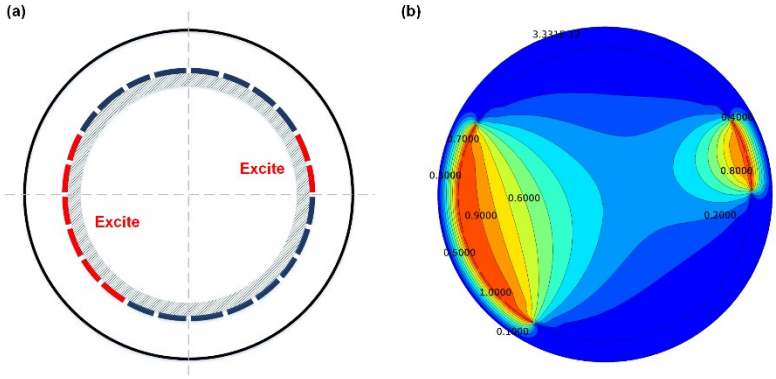

Fig. 7. Electrical potential distribution from MASS. (a) Position of the excited electrode; (b) Resulting electrical potential.

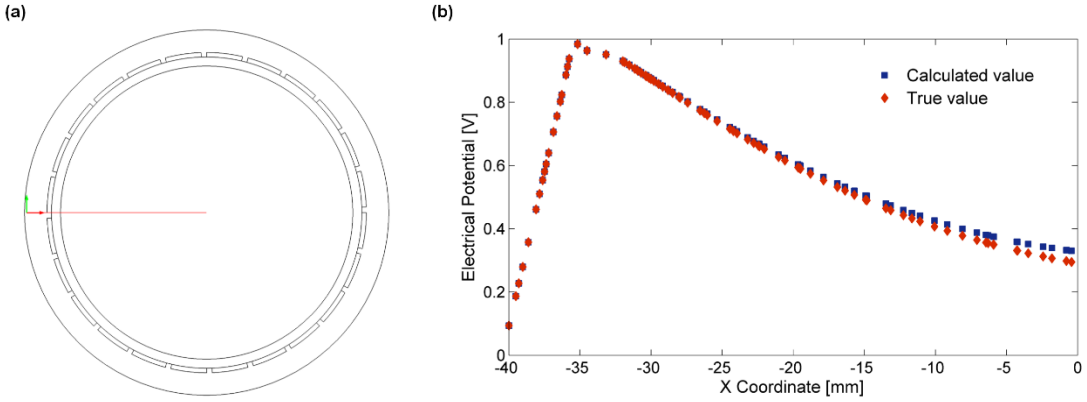

Fig. 8. Comparison of real electrical potential value and calculated value by linear superposition. (a) 1D cut line for data extraction; (b) Electrical potential value on the 1D cut line.

To characterize the MASS, following criteria are evaluated: number of capacitance measurements, compression ratio, maximum and minimum capacitance, dynamic range and sensitivity distribution. The compression ratio is defined as:

$$\alpha = n / l \tag{5}$$

where l and n are as the same definition as in Eq. (2). The compression ratio reflects the decrease of capacitance measurements through using multi-electrode sensing, and on the other hand, the acceleration of frame rate.

The dynamic range is defined as:

$$\beta = C_{\max} / C_{\min} \tag{6}$$

where $C_{\max}$ and $C_{\min}$ denote the maximum capacitance and minimum capacitance in a complete frame measurement, respectively. The dynamic range indicates the 'bandwidth' the capacitance measurement circuit needs to provide in order to perform accurate measurement on the sensor.

Fig. 9(a) shows the capacitance vector obtained from the modelled 24-electrode sensor, 12-electrode sensor and MASS respectively, for one frame image reconstruction, under the condition that the region of interest is homogenously filled with air (ε=1.0). While Fig. 9(b) illustrates the change of capacitance measurements obtained from the three sensing strategies when the region of interest are homogenously filled with sand (ε=3.0) and air,

respectively. The quantitative criteria of 24-electrode sensor, 12-electrode sensor and MASS based on simulation data are listed in Table 2.

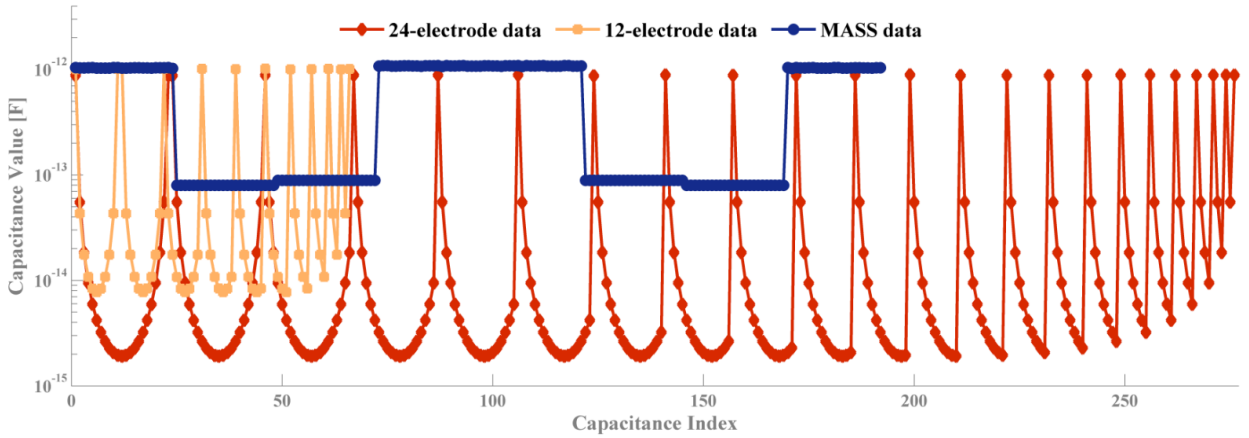

(a)

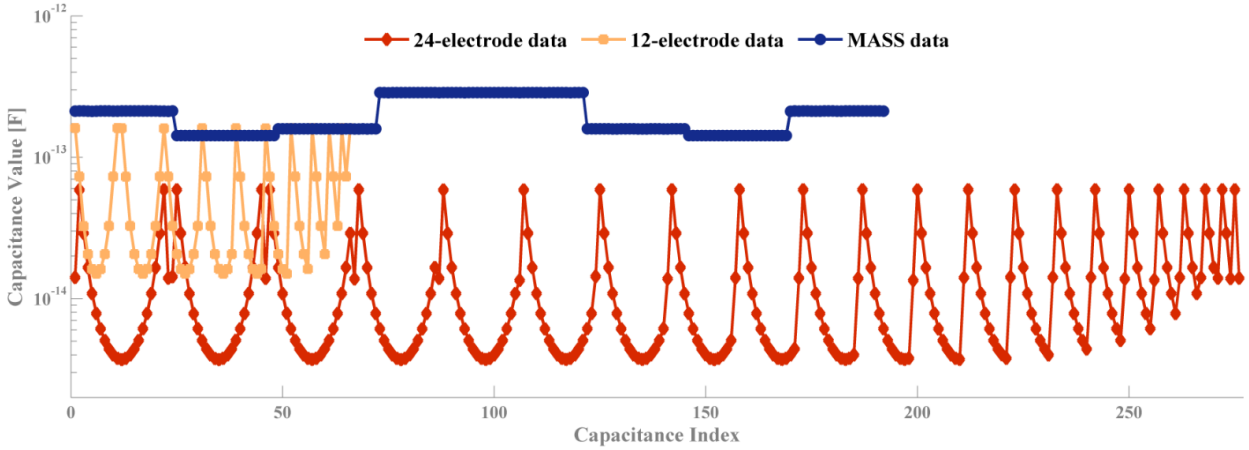

(b)

Fig. 9. Capacitance measurement vectors from simulation. (a) Absolute capacitance when the region of interest is air; (b) capacitance change when the region of interest are sand and air respectively.

Table 2. The quantitative criteria of the 24-electrode sensor, 12-electrode sensor and MASS.

Strategy \ Criteria	Number of Capacitances	Compression Ratio	Maximum Capacitance [F]	Minimum Capacitance [F]	Dynamic Range
24-electrode	276	1	8.8925e-13	1.9112e-15	465.3
12-electrode	66	1	1.0178e-12	7.7192e-15	131.9
MASS	192	1.4375	1.0893e-12	7.9780e-14	13.7

Fig. 9(a) indicates that for conventional 24-electrode and 12-electrode sensing strategies, capacitances formed by different electrode pairs vary dramatically from fF level to pF level. While for MASS, the capacitance values fall into only around three ranges. In [11], it is concluded that when conducting image reconstruction based on linearized ECT model as demonstrated in Eq. (1), different capacitance value levels have varying nonlinear effect in image reconstruction process and the image quality becomes even worse when the permittivity distribution is asymmetric. Therefore, by compressing capacitance ranges on the premise of preserving enough information, MASS is expected to have smaller image error caused by nonlinear effect. As for the capacitance variation shown in Fig. 9(b) when the region of interest are homogeneously filled with high and low permittivity medium respectively, it can be seen that the smallest variation of MASS is still above 0.1 pF, which is much larger than the other sensing strategies.

As for typical sensing strategies, the number of capacitance measurement, C_N^2, increases as the increase of electrode number *N*. Meanwhile, dynamic range also increases rapidly. As indicated in Table 2, the dynamic range of 12-electrode sensor is 131.9. However, the dynamic range increases to 465.3 when using a 24-electrode sensor and the minimum capacitance decreases from 7.7192 fF to 1.9112 fF. The large dynamic range and small capacitance will pose a large challenge for capacitance measurement system, meanwhile it is also difficult to maintain a high signal to noise ratio (SNR) for small capacitance measurement. By applying the MASS, the dynamic range is decreased to 13.7 while providing 192 measurements for one image reconstruction, which benefits accurate analogy-to-digital conversion in the ECT system. In addition, it is also possible to improve the overall SNR as the minimum capacitance is larger than 0.1 pF. Moreover, the compression ratio of MASS is 1.4375, it means that although based on a 24-electrode ECT sensor, the frame rate of MASS is accelerated to 1.4375 times faster than that of typical 24-electrode sensing strategy when using serial or semi-parallel measurement architecture based ECT systems. While with ~1.9 times more capacitance measurements, MASS can still achieve ~300 frames per second on our high-speed ECT system.

Another advantage of MASS is the improvement of sensitivity and information preservation. Fig. 10 shows the summary of sensitivity of all capacitance measurements. It indicates that the sensitivity value of MASS is much higher than that of 24-electrode and 12-electrode sensors. Moreover, the shape of the MASS sensitivity is flatter than the other two strategies, which means that even though the sensitivity value near center area is still small, the difference between the center and edge is smaller than that of 12-electrode and 24-electrode sensors.

In addition to the improved sensitivity, a crucial characteristic which makes the compression of capacitance ranges possible in MASS is the asymmetric distribution of sensitivity. Fig. 11(a), (b) and (c) show the comparison of sensitivity distributions of one measurement from 24-electrode, 12-electrode sensors and MASS, respectively. For conventional sensing strategies, sensitivity distributions are always symmetric and as a result, more projection combinations are required to obtain location and boundary information of permittivity distribution. Hence, for conventional ECT sensing strategies, it is not possible to reduce capacitance values and weaken nonlinear effect without losing any permittivity change information. Instead, the asymmetric sensitivity distribution of MASS as shown in Fig. 11(c) consists more permittivity change information in one projection thus making image reconstruction using less capacitance categories possible.

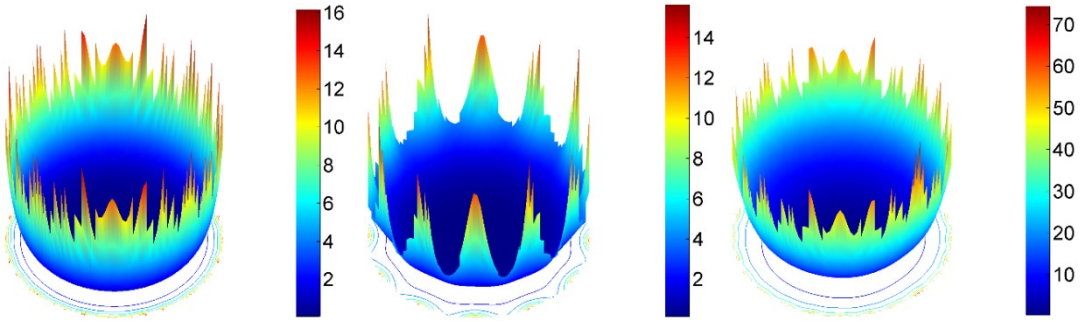

Fig. 10. Sensitivity summary. (a) 24-electrode sensor; (b) 12-electrode sensor; (c) MASS.

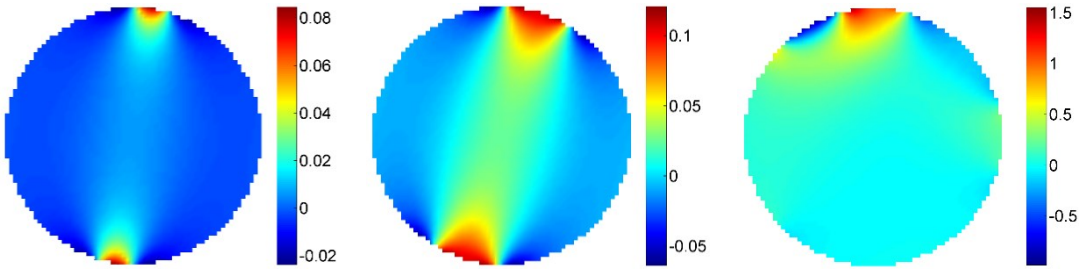

Fig. 11. Sensitivity distribution of one measurement. (a) 12-electrode sensor; (b) 24-electrode sensor; (c) MASS.

3. Results and Discussion

In this section, image reconstructions of typical permittivity distribution phantoms are carried out based on frequently-used one-step algorithm and iterative algorithm. Both simulation analysis and preliminary experimental validation are presented and discussed, and in simulation study, image quality is also quantitatively evaluated for 24-electrode strategy, 12-electrode strategy and MASS results.

3.1. Image reconstruction algorithms

As for online imaging, one-step image reconstruction algorithms based on standard Tikhonov regularization [9] and second-order Gaussian-Laplace operator based regularization [14] are employed to solve the ECT inverse problem. The algorithm is expressed as:

$$\overrightarrow{g_{est}} = \left(S^{'} \vec{S} + \mu L^{'} \vec{L}\right) \; S^{'} \vec{\lambda} \tag{7}$$

where $\overrightarrow{g_{est}}$ is the estimated permittivity vector; μ is the regularization factor; $\vec{L}$ is the second-order four-connected region Gaussian-Laplace operator matrix for the defined pixels (64×64 in this paper), and if a unit matrix is applied, this algorithm will become the standard Tikhonov regularization. The estimated permittivity of each pixel is restricted to the range [0, 1]. The implementation detail of the algorithm can be referred to our former paper [14]. Note that Eq. (7) can be applied directly to the linearized model for multi-electrode sensing given in Eq. (4) as well. To improve the real-time performance, the time-consuming part $\left(\overline{S^{'}} \vec{S} + \mu L^{'} \vec{L}\right) \; S^{'}$ can be calculated offline in advance so that there is only one matrix multiplication operation for online imaging.

In order to obtain better image quality, the most frequently-used iterative image reconstruction algorithm, i.e., projected Landweber iteration [15], is also utilized to estimate the permittivity distribution. The algorithm is expressed as:

$$\overrightarrow{g_{k+1,est}} = P\left\lfloor \overrightarrow{g_{k,est}} - \alpha S^{'} \left(S^{'} \overrightarrow{g_{k,est}} - \vec{\lambda}\right) \right\rfloor \tag{8}$$

$$P\left[f(x)\right] = \begin{cases} 0 & if \; f(x) < 0 \\ f(x) & if \; 0 \le f(x) \le 1 \\ 1 & if \; f(x) > 1 \end{cases} \tag{9}$$

where $\overrightarrow{g_{k+1,est}}$ and $\overrightarrow{g_{k,est}}$ are the permittivity estimation for the k+1 step and k step, respectively; α is the relaxation factor; P is a projection operator to restrict the reconstructed value to the range [0, 1].

To quantitatively evaluate the image quality under simulation study, two criteria [9], i.e., relative image error and correlation coefficient, are calculated for each image reconstruction result. The definitions are expressed as:

$$Relative\ image\ error = \frac{\| \overrightarrow{g_{est}} - \vec{g} \|}{\| \vec{g} \|} \tag{10}$$

$$Correlation\ coefficient = \frac{\sum_{i=1}^{M} \left(g_{i,est} - g_{avr,est}\right)\left(g_i - g_{avr}\right)}{\sqrt{\sum_{i=1}^{M} \left(g_{i,est} - g_{avr,est}\right)^2 \sum_{i=1}^{M} \left(g_i - g_{avr}\right)^2}} \tag{11}$$

where $\overrightarrow{g_{est}}$ is the estimation of permittivity distribution; $\vec{g}$ is the true permittivity distribution; $g_{i,est}$ and g_i are the i^{th} element of $\overrightarrow{g_{est}}$ and $\vec{g}$, respectively; $g_{avr,est}$ and g_{avr} are the average of $\overrightarrow{g_{est}}$ and $\vec{g}$, respectively.

3.2. Simulation study

In simulation study, four 3D permittivity phantoms are modelled to represent typical permittivity patterns in ECT applications, e.g., discrete solid particles, annular flow, stratified flow and irregular solid particles. The 3D permittivity distributions and their 2D profiles are illustrated in the first two columns of Fig. 12 respectively. For all given

phantoms, the high permittivity area (highlighted part in the figure) is filled with sand (relative permittivity equals to 3.0) while the low permittivity area is filled with air (relative permittivity equals 1.0). Reconstructions using 24-electrode data, 12-electrode data and MASS data are performed for evaluation and comparison purpose. All reconstructed images and phantoms are presented in a normalized form with the result of each pixel restricted within [0, 1].

Fig. 12 shows the image reconstruction results and their corresponding quantitative evaluation on the basis of the one-step algorithm given in Eq. (7) and noise-free data. The one-step image reconstruction algorithm is suitable for real-time applications because of its low computational cost whilst offers only qualitative estimation of permittivity distribution with low image quality and resolution. The results obtained indicate that the MASS can deliver much better image quality for the first three permittivity phantoms and comparable image quality for the last permittivity phantom, compared with the 24-electrode and 12-electrode sensing strategies. Additionally, the feasibility of online imaging using MASS is also verified.

Phantom		24-electrode	12-electrode	MASS
3D	2D			
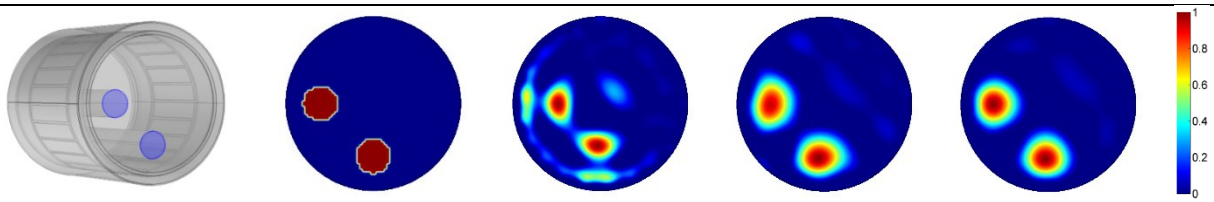				
μ in Eq. (7)		0.001	0.001	0.001
Image error [%]		80.86	52.95	47.76
Correlation coefficient		0.5570	0.8393	0.8736
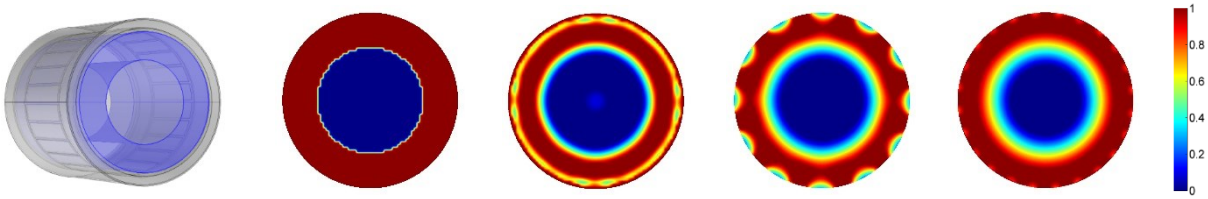				
μ in Eq. (7)		0.001	0.001	0.001
Image error [%]		24.19	26.58	23.49
Correlation coefficient		0.9290	0.9076	0.9257
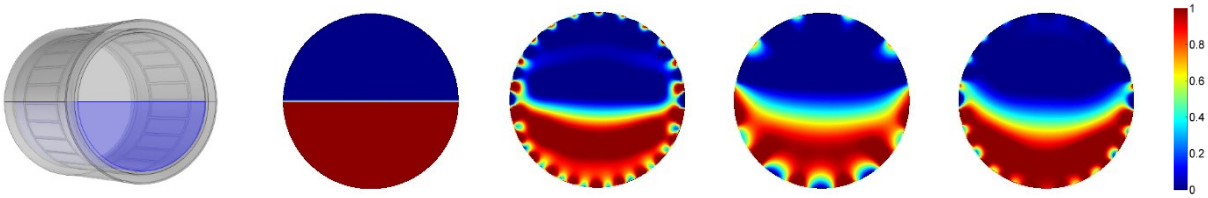				
μ in Eq. (7)		0.001	0.001	0.001
Image error [%]		40.56	39.18	38.82
Correlation coefficient		0.8316	0.8588	0.8582
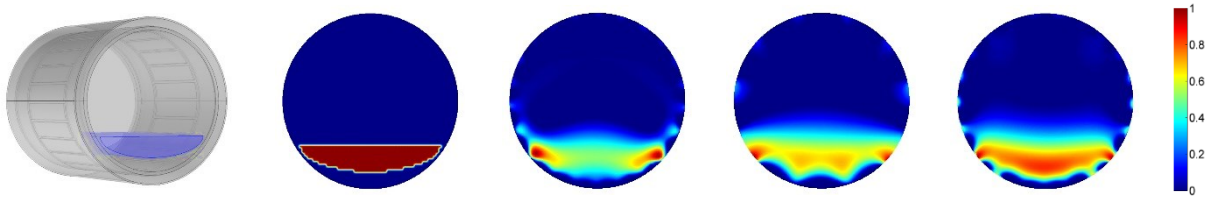				
μ in Eq. (7)		0.001	0.001	0.001
Image error [%]		56.69	60.89	58.18
Correlation coefficient		0.8284	0.7662	0.7946

Fig. 12. Image reconstruction results using the one-step algorithm.

As the one-step image reconstruction algorithm is mainly for online qualitative imaging, reconstructions using the iterative algorithm as given in Eq. (8) are also performed to deliver better image quality and noise reduction. Fig. 13 shows the reconstruction results and quantitative evaluation using projected Landweber iteration and noise-free data. A maximum iteration number of 2000 and a stop rule of minimum image error are adopted for all phantoms during the implementation.

Phantom		24-electrode	12-electrode	MASS
3D	2D			
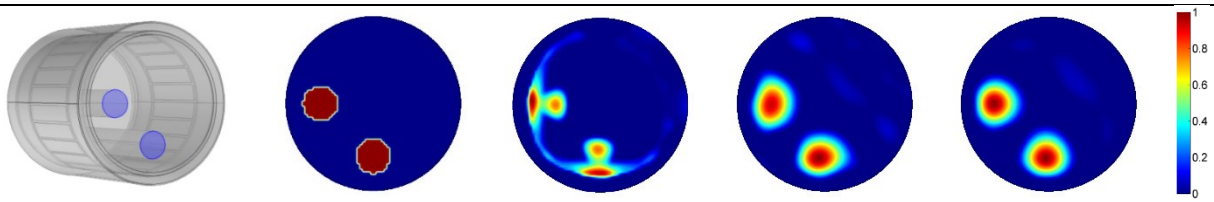				
α in Eq. (8)		0.5	0.5	0.5
Iteration		1346	55	21
Image error [%]		68.67	51.91	46.85
Correlation coefficient		0.7266	0.8525	0.8858
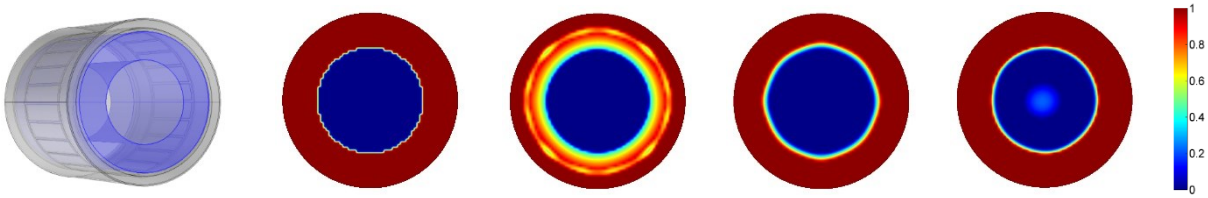				
α in Eq. (8)		1	1	1
Iteration		276	2000	2000
Image error [%]		23.92	18.80	10.28
Correlation coefficient		0.9387	0.9532	0.9861
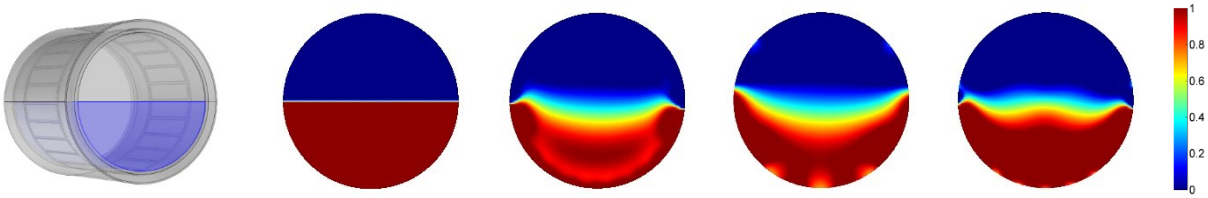				
α in Eq. (8)		0.5	0.5	0.5
Iteration		52	185	804
Image error [%]		28.90	30.23	23.94
Correlation coefficient		0.9266	0.9115	0.9447
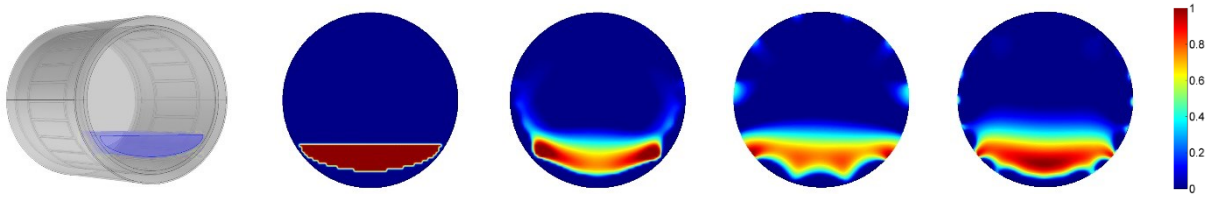				
α in Eq. (8)		0.5	0.5	0.5
Iteration		104	103	41
Image error [%]		45.69	59.64	55.55
Correlation coefficient		0.8785	0.7824	0.8218

Fig. 13. Image reconstruction results using the projected Landweber iteration algorithm.

It is found that, for the relatively sparse permittivity phantom, such as discrete solid particles in the first row, there are evident boundary distortion in 12-electrode reconstruction, and it is even worse in 24-electrode result; while the boundary of reconstructions using MASS are more accurate and image error is smaller as well. Regarding the

symmetric permittivity phantom, such as annular flow in the second row, all strategies can obtain high quality images with small image errors. However, by compressing capacitance dynamic range, the MASS is able to get even better image with clearer boundary. For the most challenging permittivity phantom, such as stratified flow in the third row and the irregular solid particles in the last row, reconstructions using 12-electrode strategy suffer a curved and blurred interface between the high dielectric medium and air, and evident artefact spots can be found near the pipe wall. While for results using MASS, image quality is greatly improved with a more flat interface and less artefact spots, which indicates weaker nonlinear effect. From the comparison of images and quantitative evaluation results, it can be concluded that MASS has superior performance in weakening nonlinear effect and thus being able to produce tomographic images with higher quality.

Fig. 14 illustrates the change of relative error versus iteration number of reconstructions in Fig. 13. For the phantom in row 1 and row 4, MASS converges to the minimal error faster than other methods. While for the phantom in row 2, relative image errors of MASS continue to reduce with respect to the iteration number, which demonstrates smaller linearized error. With regard to the stratified flow phantom in row 3, for conventional 24-electrode and 12-electrode strategy, there is hardly any image quality improvement using iterative method due to its highly nonlinear characteristics. However, a significant decrease of image error versus iteration can be seen by using MASS, which demonstrates weaker nonlinear effect.

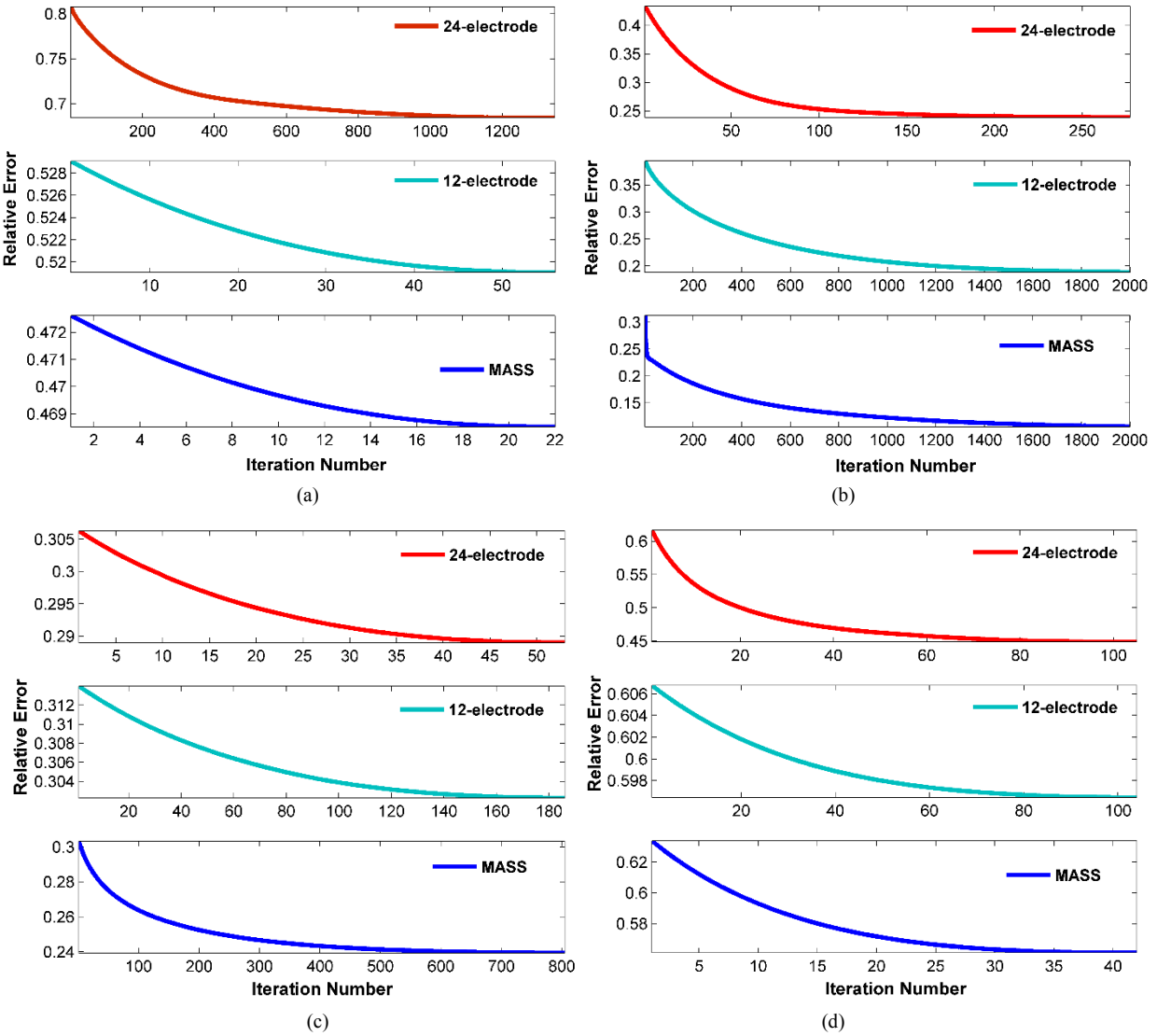

Fig. 14. Iteration number vs relative image error. (a) Phantom 1; (b) Phantom 2; (c) Phantom 3; (d) Phantom 4.

3.3. Experimental study

To further validate the feasibility of MASS in real practice, a series of static experiments were carried out. A 24-electrode ECT sensor was designed and manufactured using flexible printed circuit, which design and installation are shown in Fig. 15(a), (b) and (c) respectively. In addition, a typical 12-electrode sensor was also manufactured for comparison, which picture is illustrated in Fig. 15(d). The ID of the pipes is 75 mm and material is PVC.

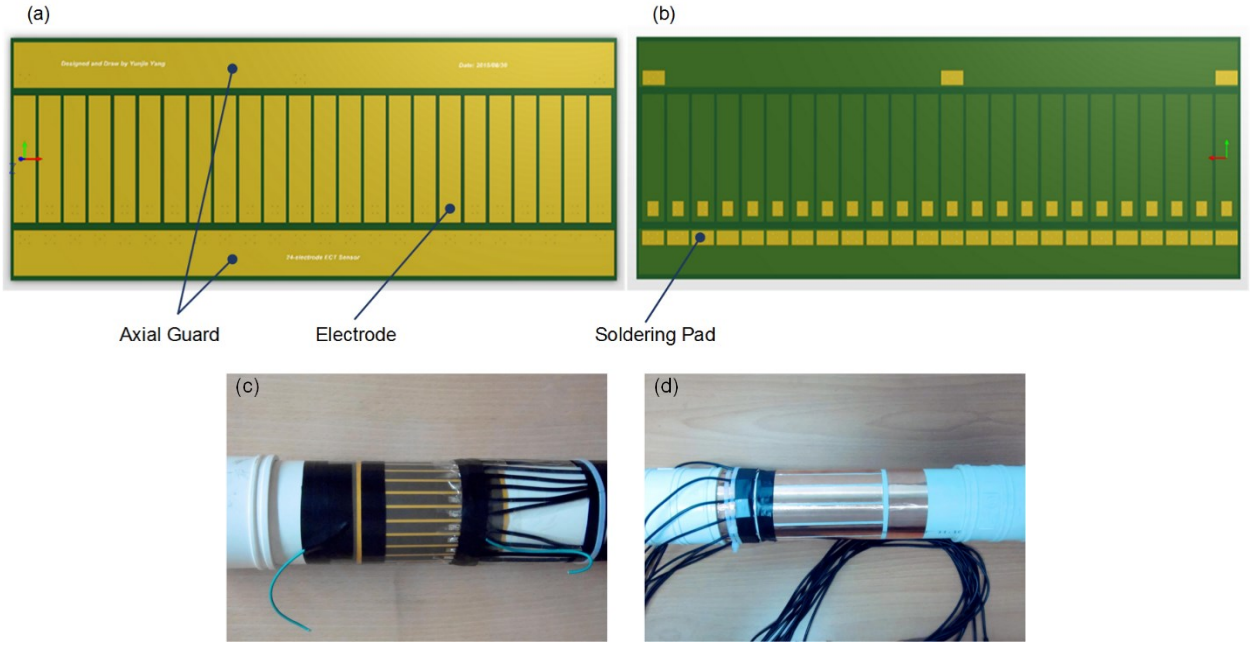

Fig. 15. 24-electrode and 12-electrode sensors for experiments. (a) front view of the 24-electrode sensor design; (b) back view of the 24-electrode sensor design; (c) picture of the 24-electrode sensor; (d) picture of the 12-electrode sensor.

A high-speed and sensing-strategy configurable ECT system together with a visualization and control software have been developed to enable flexible ECT sensing. This software supports interactive design of arbitrary sensing strategy with up to 32 electrodes. The system hardware and software interface are shown in Fig. 16(a) and (b). The AC-based method [16] is applied to measure capacitance and the excitation frequency and peak-peak amplitude are set as 200 kHz and 15 V, respectively. Under the user-defined mode in software, the customized sensing strategy can be configured instead of directly using typical sensing strategy. After designing or loading the user-defined sensing strategy, the linear superposition matrix $\vec{L}$ and new sensitivity matrix $\overline{S_m}$ in Eq. (3) and Eq. (4) will be calculated and a switch array control matrix will be generated and downloaded to the ECT instrument accordingly.

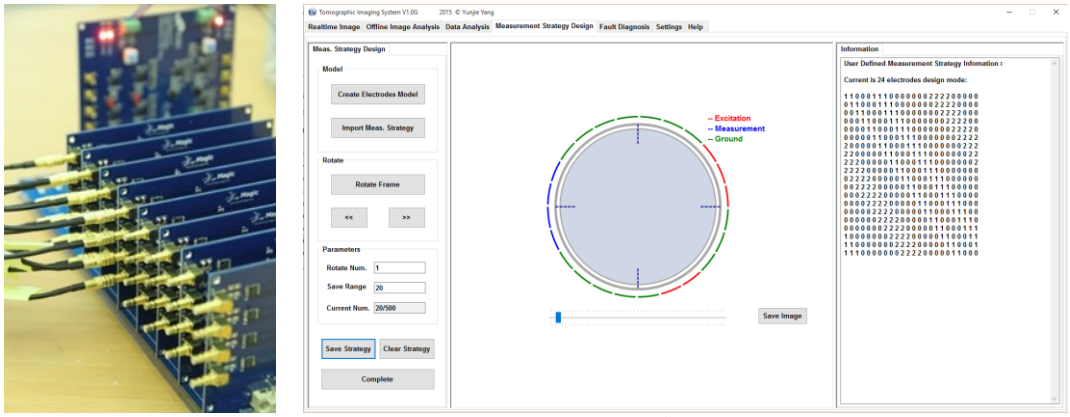

(a) (b)

Fig. 16. The developed ECT system supporting flexible sensing strategy. (a) ECT instrument; (b) sensing strategy design interface of visualization and control software.

The experiments of three practical permittivity phantoms, e.g., discrete solid particles with different dielectric constants (PVC and wax rods respectively), annular flow and stratified flow as shown in the first column of Fig. 17, are conducted. For practical purpose, only 12-electrode sensing and MASS sensing for the given phantoms are performed for image reconstruction. For iterative algorithm, fixed iteration numbers, i.e., 200 for discrete solid particles and annular flow, and 20 for stratified flow, are applied. Image reconstruction results using one-step and iterative algorithms given by Eq. (7) and Eq. (8) are illustrated in Fig. 17, and it is shown that the results based on experimental data coincide well with the simulation analysis, which further demonstrates MASS is a favorable alternative ECT sensing strategy.

Test Phantom	One-step Algorithm		Iterative Algorithm	
	12-electrode	MASS	12-electrode	MASS
	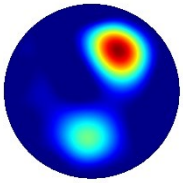	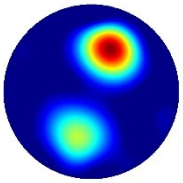	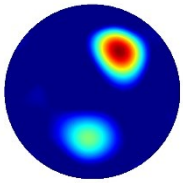	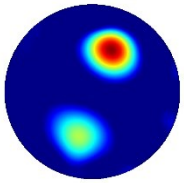 
μ in Eq. (7)	0.0005	0.0005	NA	NA
α in Eq. (8)	NA	NA	10	10
Iteration	NA	NA	200	200
	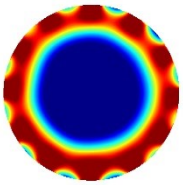	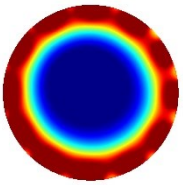	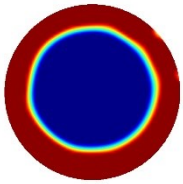	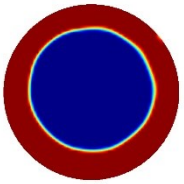 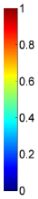
μ in Eq. (7)	0.0005	0.0005	NA	NA
α in Eq. (8)	NA	NA	10	10
Iteration	NA	NA	200	200
	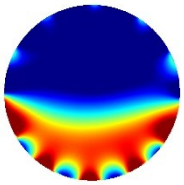	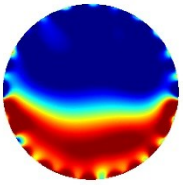	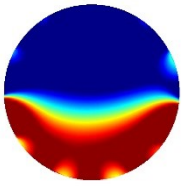	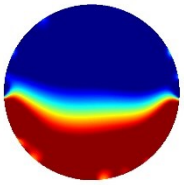 
μ in Eq. (7)	0.0005	0.0005	NA	NA
α in Eq. (8)	NA	NA	10	10
Iteration	NA	NA	20	20

Fig. 17. Image reconstruction results using experimental data.

4. Conclusion

Targeting at the bottleneck of existing ECT sensor and sensing strategy, this paper investigates the possibility of utilizing multi-electrode simultaneous excitation sensing from fundamental theory to experimental validation. A novel multi-electrode asymmetric sensing strategy (MASS) with ultra-low dynamic range is developed, characterized, and verified through both simulation study and experiments. In order to further decrease dynamic range and capacitance categories, multi-electrode simultaneous excitation and measurement scheme is proposed. Meanwhile, asymmetric electrode structure is introduced to induce an asymmetric sensitivity field, which is able to preserve more information of permittivity change in one projection compared with typical symmetric sensitivity distribution. By taking advantage of the asymmetric sensitivity field and opposite multi-electrode excitation scheme, it is proved that the dynamic range of capacitance measurements can be decreased to around 13.7 and capacitance categories are reduced to around three by value levels. As MASS generates more capacitance data (192) compared with the common 12-electrode strategy (66), the sampling speed will be around 3 times slower. For our developed digital ECT system, the frame rate is able

to achieve as high as 890 frames per second. Therefore, the proposed strategy can still be applied in real-time applications with a maximum frame rate of around 263 frames per second. The benefits of MASS have been validated by simulation and experiment, which results indicate that the quality of reconstruction images can be significantly improved for typical permittivity phantoms. In addition, attributing to its small dynamic range, MASS has lower requirement for capacitance measurement system development, which will make it easier to construct a high performance ECT system.

Future work will focus on the application of MASS in dynamic experiments and industrial field and exploring the possibility of extending such technique in other electrical tomography modalities, for instance, electrical impedance tomography.

Acknowledgements

The authors would like to thank 2015 IEEE I&M Society Graduate Fellowship Award for partially support this work.

References

[1] Xie, C. G., Huang, S. M., Beck, M. S., Hoyle, B. S., Thorn, R., Lenn, C., & Snowden, D. (1992). Electrical capacitance tomography for flow imaging: system model for development of image reconstruction algorithms and design of primary sensors. *IEE Proceedings G (Circuits, Devices and Systems)*, *139*(1), 89-98.

[2] Wang, H., & Yang, W. (2011). Scale-up of an electrical capacitance tomography sensor for imaging pharmaceutical fluidized beds and validation by computational fluid dynamics. *Measurement Science and Technology*, *22*(10), 104015.

[3] Li, Y., Yang, W., Xie, C. G., Huang, S., Wu, Z., Tsamakis, D., & Lenn, C. (2013). Gas/oil/water flow measurement by electrical capacitance tomography. *Measurement Science and Technology*, *24*(7), 074001.

[4] Xue, Q., Wang, H., Yang, C., & Cui, Z. (2012). Dynamical lag correlation exponent based method for gas–solid flow velocity measurement using twin-plane electrical capacitance tomography. *Measurement Science and Technology*, *23*(8), 085301.

[5] Gut, Z., & Wolanski, P. (2010). Flame imaging using 3D electrical capacitance tomography. Combustion Science and Technology, 182(11-12), 1580-1585.

[6] Cui, Z., Wang, H., Chen, Z., Xu, Y., & Yang, W. (2011). A high-performance digital system for electrical capacitance tomography. *Measurement Science and Technology*, *22*(5), 055503.

[7] Yang, Y., & Peng, L. (2013). A configurable electrical capacitance tomography system using a combining electrode strategy. *Measurement Science and Technology*, *24*(7), 074005.

[8] Olmos, A. M., Carvajal, M. A., Morales, D. P., García, A., & Palma, A. J. (2008). Development of an electrical capacitance tomography system using four rotating electrodes. *Sensors and Actuators A: Physical*, *148*(2), 366-375.

[9] Yang, W. Q., & Peng, L. (2003). Image reconstruction algorithms for electrical capacitance tomography. *Measurement Science and Technology*, *14*(1), R1.

[10] Wang, H., Tang, L., & Cao, Z. (2007). An image reconstruction algorithm based on total variation with adaptive mesh refinement for ECT. *Flow Measurement and Instrumentation*, *18*(5), 262-267.

[11] Yang, Y., & Peng, L. Y. (2013). Data pattern with ECT sensor and its impact on image reconstruction. *Sensors Journal, IEEE*, *13*(5), 1582-1593.

[12] Ye, J., Wang, H., & Yang, W. (2015). Image reconstruction for electrical capacitance tomography based on sparse representation. *Instrumentation and Measurement, IEEE Transactions on*, *64*(1), 89-102.

[13] Peng, L., Ye, J., Lu, G., & Yang, W. (2012). Evaluation of effect of number of electrodes in ECT sensors on image quality. *Sensors Journal, IEEE*, *12*(5), 1554-1565.

[14] Yang, Y., Jia, J., Polydorides, N., & McCann, H. (2014, October). Effect of structured packing on EIT image reconstruction. In *Imaging Systems and Techniques (IST), 2014 IEEE International Conference on* (pp. 53-58). IEEE.

[15] Yang, W. Q., Spink, D. M., York, T. A., & McCann, H. (1999). An image-reconstruction algorithm based on Landweber's iteration method for electrical-capacitance tomography. *Measurement Science and Technology*, *10*(11), 1065.

[16] Yang, W. Q., & York, T. A. (1999). New AC-based capacitance tomography system. *IEE Proceedings-Science, Measurement and Technology*, *146*(1), 47-53.